ADVANCED FUNCTIONAL MATERIALS
www.afm-journal.de

A Computational Framework to Accelerate the Discovery of Perovskites for Solar Thermochemical Hydrogen Production: Identification of Gd Perovskite Oxide Redox Mediators

*Zachary J. L. Bare, Ryan J. Morelock, and Charles B. Musgrave**

A high-throughput computational framework to identify novel multinary perovskite redox mediators is presented, and this framework is applied to discover the Gd-containing perovskite oxide compositions $Gd_2BB'O_6$, $GdA'B_2O_6$, and $GdA'BB'O_6$ that split water. The computational scheme uses a sequence of empirical approaches to evaluate the stabilities, electronic properties, and oxygen vacancy thermodynamics of these materials, including contributions to the enthalpies and entropies of reduction, ΔH_{TR} and ΔS_{TR}. This scheme uses the machine-learned descriptor τ to identify compositions that are likely stable as perovskites, the bond valence method to estimate the magnitude and phase of BO_6 octahedral tilting and provide accurate initial estimates of perovskite geometries, and density functional theory including magnetic- and defect-sampling to predict STCH-relevant properties. Eighty-three promising STCH candidate perovskite oxides down-selected from 4392 Gd-containing compositions are reported, three of which are referred to experimental collaborators for characterization and exhibit STCH activity. The results demonstrate that the high-throughput computational scheme described herein—which is used to evaluate Gd-containing compositions but can be applied to any multinary perovskite oxide compositional space(s) of interest—accelerates the discovery of novel STCH active redox mediators with reasonable computational expense.

1. Introduction

Solar thermochemical hydrogen (STCH) production is a promising method to generate carbon neutral fuels from water using concentrated solar energy.[1,2] STCH is typically produced by either low-temperature, multistep processes or high-temperature, two-step processes.[3] Although some notable multistep STCH processes have been demonstrated,[4] these methods involve design complications and inefficiencies such that two-step STCH processes are now generally preferred.[5] Two-step STCH processes involve a reducible metal oxide, referred to as a redox mediator, that facilitates the dissociation of steam. These processes begin with a high-temperature thermal reduction step ($T_{TR} \leq 1500$ °C) to reduce the redox mediator, resulting in a phase change and/or partial reduction of the mediator. The reduction step is followed by the oxidation step, which splits water and is typically performed at lower temperatures ($T_{WS} \geq 850$ °C), during which steam reoxidizes the redox mediator and, in the process, generates hydrogen gas.[6–8] The gold standard STCH redox mediator, CeO_2, exhibits rapid oxidation kinetics, long-term cyclability, and consistent H_2 production at low steam-to-H_2 ratios, all of which are desirable for STCH.[9,10] However, CeO_2 also suffers from low H_2 yields at reduction temperatures $T_{TR} \leq 1500$ °C, the practical operating temperature limit for conventional reactor materials, which limits its use in industrial applications. The development of novel redox mediators that exhibit enhanced water-splitting performances at lower temperatures ($T_{TR} < 1500$ °C) is therefore critical for the commercial viability of STCH production.

The perovskite oxide chemical space provides a large and promising source of potential STCH redox mediators.[11] Single perovskite oxides (ABO_3 compositions) have the same crystal structure as the prototypical mineral perovskite $CaTiO_3$, in which large radii A-site cations occupy the same sites as Ca, smaller radii B-site cations occupy the octahedrally coordinated sites of Ti, and O occupies the corners of the corner-sharing octahedra. Complex perovskite oxides

Z. J. L. Bare, R. J. Morelock, C. B. Musgrave
Department of Chemical and Biological Engineering
University of Colorado Boulder
Boulder, CO 80309, USA
E-mail: charles.musgrave@colorado.edu
C. B. Musgrave
Renewable and Sustainable Energy Institute
University of Colorado Boulder
Boulder, CO 80309, USA
C. B. Musgrave
Materials Science and Engineering Program
University of Colorado Boulder
Boulder, CO 80309, USA

The ORCID identification number(s) for the author(s) of this article can be found under https://doi.org/10.1002/adfm.202200201.

DOI: 10.1002/adfm.202200201

with $A_xA'_{1-x}B_yB'_{1-y}O_3$ compositions, such as $BaCe_{0.25}Mn_{0.75}O_3$ (BCM)[12] and $Sr_{0.4}La_{0.6}Mn_{0.4}Al_{0.6}O_3$ (SLMA),[11,13,14] were previously demonstrated as redox mediators for STCH, and exhibit improved redox cyclability relative to redox mediators that operate by a phase change mechanism, such as Fe_3O_4,[15] and lower reduction temperatures relative to CeO_2. Perovskite oxides are an attractive STCH materials space due to the expected diverse and tunable[16] properties of the many different compositions that adopt the perovskite structure,[17] which include high-temperature stability, reducibility, high ionic conductivity, and facile reoxidation.[18] However, currently known STCH active perovskites suffer from low hydrogen production capacities and slow oxidation kinetics, which have impeded the development of these materials as redox mediators for commercial-scale STCH processes. Identifying novel perovskite oxide compositions with improved H_2 production capacity and rapid reduction and oxidation kinetics continues to be a primary goal of the STCH community.

Thermodynamic analysis by Muhich et al. and others showed that viable STCH redox materials must satisfy the following STCH Gibbs free energy inequalities[5,19]

$$\Delta H_{\text{cycle}} = \Delta H_{\text{TR}} + \Delta H_{\text{WS}} \geq 286 \text{ kJ/mol} \tag{1}$$

$$\Delta S_{\text{cycle}} = \Delta S_{\text{TR}} + \Delta S_{\text{WS}} \geq 44.4 \text{ J/mol K} \tag{2}$$

Ideal STCH redox mediators possess a reduction enthalpy, ΔH_{TR}, large enough to reduce steam, but not so large that excessively high temperatures are required to reduce the mediator.[19] In contrast, maximizing the reduction entropy, ΔS_{TR}, benefits both requirements, as large ΔS_{TR} decreases the free energy of reduction at a given temperature and therefore lowers the temperature necessary to reduce a material with a given ΔH_{TR}. Recent investigations of STCH active materials have characterized contributions to ΔS_{TR}. For instance, Naghavi et al. showed that the state-of-the-art STCH redox material CeO_2 exhibits a "giant," positive onsite electronic entropy of reduction, $\Delta S_{\text{TR,elec}}$,[20] in addition to configurational and vibrational entropies associated with oxygen vacancy formation.[21] Ceria's large $\Delta S_{\text{TR,elec}}$ arises from the multiplicity of unoccupied Ce f-orbital states that lie near the conduction band minimum (CBM), which become thermally accessible relative to the Fermi level of CeO_2 at STCH reduction temperatures. This insight led to the identification of $CeTi_2O_6$ as a STCH active redox material following a computational investigation of Ce-containing oxides by Naghavi et al.[22]

More generally, Lany et al. showed that the formation of charged oxygen vacancy defects under STCH reduction conditions results in large $\Delta S_{\text{TR,elec}}$ if a material possesses a large density of states (DOS) electron effective mass, denoted as m_e^*, near the CBM.[23] m_e^* quantifies the multiplicity of states in a manner that is not Ce f-orbital specific, meaning that the contributions to the multiplicity of states from other elements are also considered. Larger m_e^* corresponds with larger $\Delta S_{\text{TR,elec}}$, and can be rapidly and accurately characterized using first-principles electronic structure calculations such as density functional theory (DFT). Oftentimes, the evaluation of $\Delta S_{\text{TR,elec}}$ incurs no additional computational expense relative to first-principles bulk stability screening, which is typically performed in computational studies of theoretical perovskite oxides prior to experimental STCH characterization to assess the likelihood that a metal oxide composition is synthesizable and phase stable as a perovskite.[24,25] In this manner, the evaluation of m_e^* and $\Delta S_{\text{TR,elec}}$ can be efficiently integrated into high-throughput computational frameworks for STCH candidate discovery.

Herein, we demonstrate that perovskite oxides with the lanthanides Ce, La, and Gd possess large m_e^* and thus, potentially large $\Delta S_{\text{TR,elec}}$. While Ce- and La-based perovskites have previously demonstrated STCH redox activity,[12,13,26,27] Gd-based perovskites are relatively unexplored for STCH; some La-containing, STCH-active perovskite oxides retain their STCH activity when Gd is substituted for La,[28] but to our knowledge, no high-throughput computational investigations specific to the STCH activity of Gd-containing perovskites have been performed. Therefore, we focused our computational investigation on the set of theoretical Gd-containing multinary perovskite oxides with compositions $Gd_2BB'O_6$, $GdA'B_2O_6$, and $GdA'BB'O_6$, and predicted their STCH activity using a combination of ab initio and empirical approaches to evaluate the stabilities, electronic properties, and oxygen vacancy thermodynamics of these materials. Eighty-three promising STCH candidate oxides were identified from the 4392 $GdA'BB'O_6$ compositions we evaluated, which were referred to our experimental collaborators for synthesis and characterization. Of those, three were selected for synthesis and characterization over the other 80 Gd-containing candidates because they span a range of stabilities and oxygen vacancy enthalpies, which is useful for validating our choice of screening criteria. Of those, $GdLaCoFeO_6$ (GLCF), $GdLaMnNiO_6$ (GLMN), and $SrGdMnAlO_6$ (SGMA) were first synthesized because similar compositions have reported perovskite synthesis procedures. STCH activity was experimentally demonstrated for these three Gd-containing perovskites identified by our framework.[29–31] This demonstrates that the high-throughput materials discovery scheme we have developed—which evaluates perovskite/nonperovskite synthesizability, ΔH_{TR}, and $\Delta S_{\text{TR,elec}}$ using the m_e^* of complex Gd-containing perovskites—accelerates the discovery of novel STCH materials with reasonable computational expense.

2. Results and Discussion

2.1. Large m_e^* Attributable to Gd^{3+}

2.1.1. Cation Contributions to m_e^*

Perovskite oxides that possess large m_e^* should by extension exhibit larger $\Delta S_{\text{TR,elec}}$ relative to perovskite oxides with smaller m_e^*. Previous studies have shown that certain cation species (e.g., Ce^{4+}) contribute large numbers of electronic states to the DOS near the CBM of metal oxides, which can result in large m_e^*. To quantify contributions to m_e^* on a cation-by-cation basis, we evaluated the m_e^* of all available metal oxides, including nonperovskites, tabulated in the Materials Project (MP) database.[29] The MP currently contains the DFT-computed structures and energies of >140 000 inorganic materials with ≈70 000 of these entries being metal oxides. Of these,

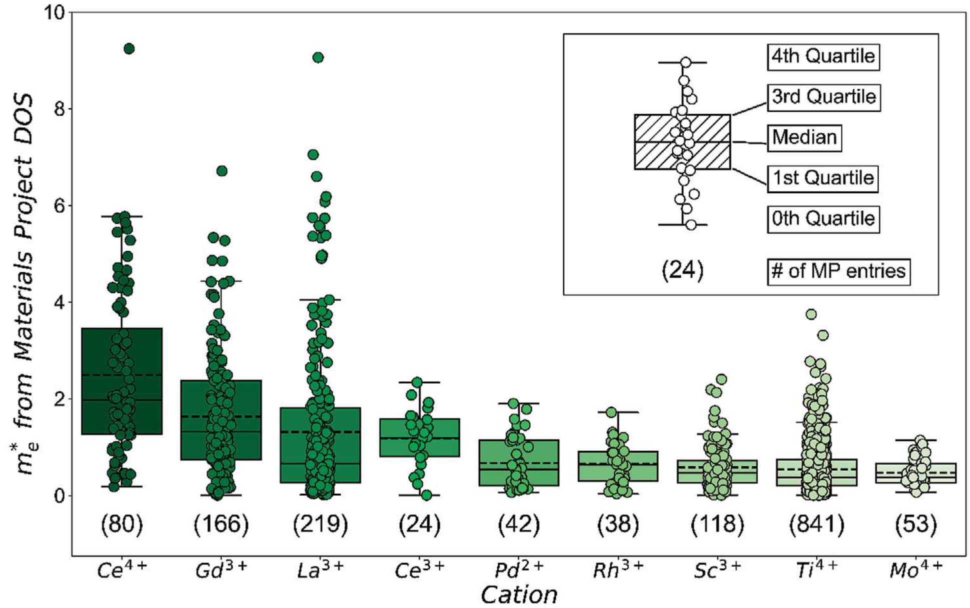

Figure 1. Distributions of m_e^* for the nine cations present in Materials Project tabulated oxides that, on average, have the largest m_e^* (only the cations present in at least 20 MP entries with tabulated DOS are reported). Cations are ordered by their mean m_e^* (black dashed line) from left to right. MP entries containing the cations Ce^{4+}, Gd^{3+}, La^{3+}, and Ce^{3+} are predicted to have the largest average m_e^* s ($\bar{m}_e^*$ = 2.485, 1.633, 1.313, and 1.180, respectively). Numbers in parentheses below the box plots denote the number of entries evaluated that contain the associated cation.

≈24 000 metal oxides possess tabulated electronic structure information from which m_e^* can be computed. To make the following analysis cation specific, we assigned oxidation states to elements present in the MP-tabulated perovskite oxides using the pymatgen[30] python package's oxidation state assignment algorithm. In this manner, we identified the cations that produce the largest m_e^* among the cations present in MP entries with tabulated DOS.

Figure 1 plots the distributions of m_e^* for the 23 723 MP metal oxides with tabulated DOS. The horizontal axis shows the nine cations present in at least 20 MP entries with tabulated DOS that have the largest mean m_e^*. Notably, Ce^{4+} is rediscovered as the cation that, on average, contributes the largest density of accessible electronic states near the CBM at 1000 K, followed by the lanthanide cations Gd^{3+}, La^{3+}, and Ce^{3+} in decreasing order. MP entries containing these four cations are computed to possess larger average m_e^* than MP entries containing the 86 other cations considered (see Table S1, Supporting Information), which suggests that one or more of these cations should be included in STCH metal oxide candidate compositions to increase ΔS_{TR}. This analysis identifies the cations that, on average, result in the largest m_e^*, but does not quantify changes in the m_e^* if one cation is substituted for another. Additionally, the data analyzed constitutes all metal oxide entries tabulated by the MP, as opposed to specifically evaluating the perovskite oxide structures. This suggests that Gd^{3+} substitution in metal oxide compositions could increase ΔS_{TR} regardless of geometry. However, as this investigation is focused on perovskites, we leveraged our ABO_3 perovskite dataset to isolate contributions to the m_e^* attributable to single cation substitutions in perovskite oxides. Our data set consists of 657 single perovskite oxide compositions generated in up to six unique perovskite geometries as denoted by their Glazer tilt notation.[31] A complete description of the ABO_3 data set used and the criteria enforced to create the substitution matrices are detailed in the Supporting Information ("ABO_3 Perovskite Dataset and Substitution Matrices").

2.1.2. +3 Cation Contributions to m_e^*: ABO_3 Perovskite Oxides

Figure 2 displays the average shifts in the m_e^* following the replacement of starting +3 cations (vertical axis) with substituted +3 cations (horizontal axis). This matrix shows that, on average, substitution of nearly all +3 cations present in our dataset by Ce^{3+} or Gd^{3+} increases m_e^*. Consistent with the MP analysis described above, substitution of Ce^{3+} by Gd^{3+} also increases m_e^* on average. Substitutions by La^{3+} generally increase m_e^* when La^{3+} is substituted for other lanthanide +3 cations, e.g., Tb^{3+}, Yb^{3+}, Pr^{3+}, etc. Therefore, our ABO_3 perovskite dataset confirms the trends in m_e^* uncovered in the MP tabulated metal oxides reported in Section 1 (Figure 1), which suggests that to maximize m_e^* for STCH applications, perovskite oxides should preferentially include one or more of the +3 lanthanides Ce^{3+}, Gd^{3+} and La^{3+}. Additional details regarding the substitution matrix, as well as matrices for +2 and +4 cation substitutions present in our dataset, are reported in the Supporting Information ("ABO_3 Perovskite Dataset and Substitution Matrices"). Because the Ce- and La-containing compositional spaces possess known STCH redox mediators that have been previously characterized, we examined the largely unexplored Gd-containing compositional space and identified several novel STCH perovskite oxides. As described in Section II, our high-throughput computational screening approach combines the machine-learned descriptor τ, the empirical bond valence method (BVM), and DFT into the scheme illustrated in **Figure 3**.

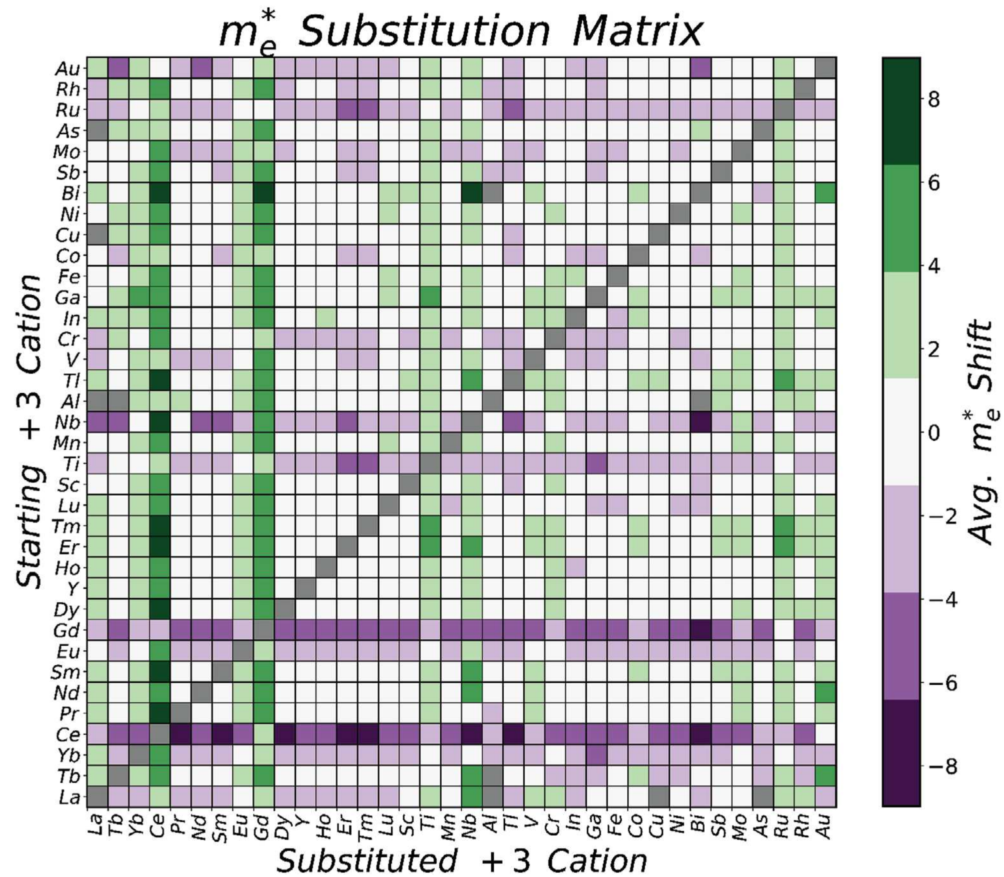

Figure 2. Substitution matrix showing the average shift in the m_e^* upon substitution of the starting A-site cation (vertical axis) with a substituted cation (horizontal axis) for the 657 ABO_3 perovskite oxides in our database. Green indicates an increase in m_e^* following substitution, whereas purple indicates a decrease in m_e^*. Cations that cannot be interchanged because the ABO_3 substitution criteria are not satisfied (see "ABO_3 Perovskite Dataset and Substitution Matrices," Supporting Information) are colored gray. Substitutions of nearly all +3 cations present in our dataset by Ce^{3+} or Gd^{3+} (fourth and ninth columns, respectively) increase m_e^*. On average, Gd^{3+} substitutions for Ce^{3+} increase the m_e^* in the ABO_3 perovskite oxides considered.

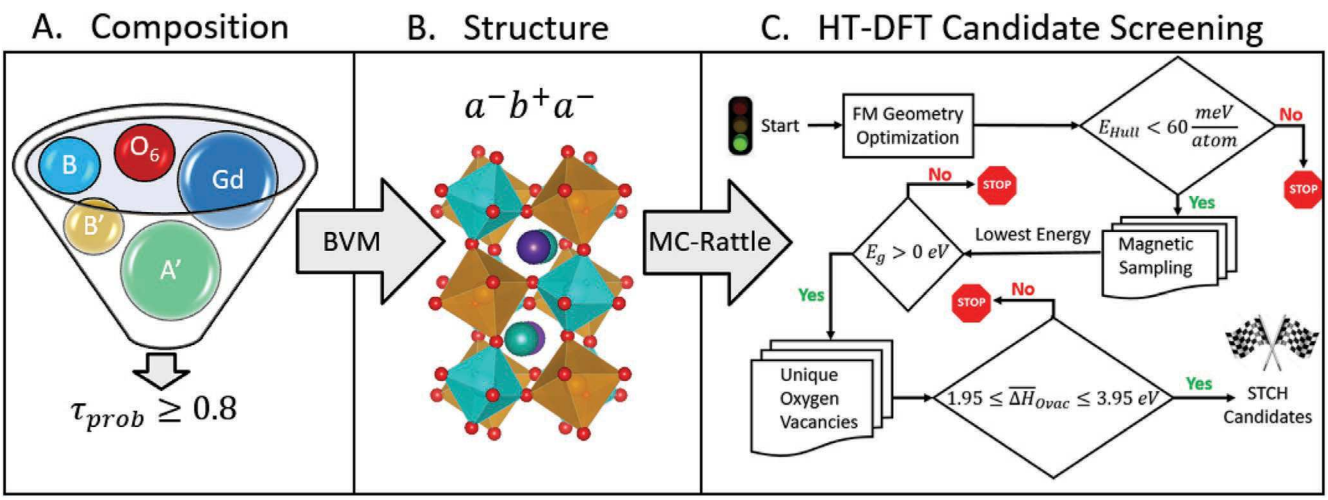

Figure 3. Schematic of the high-throughput computational approach used to identify candidate perovskite oxides for STCH from 4392 $Gd_2BB'O_6$, $GdA'B_2O_6$, and $GdA'BB'O_6$ compositions. A) Step 1: Compositional screening for perovskite stability using the machine-learned descriptor τ. B) Step 2: Determination of perovskite geometry, i.e., Glazer octahedral tilt system, using the BVM to eliminate unstable polymorphs and provide accurate initial structures for DFT geometry optimization. C) Step 3: Evaluations of stabilities, electronic properties, and oxygen vacancy enthalpies using DFT.

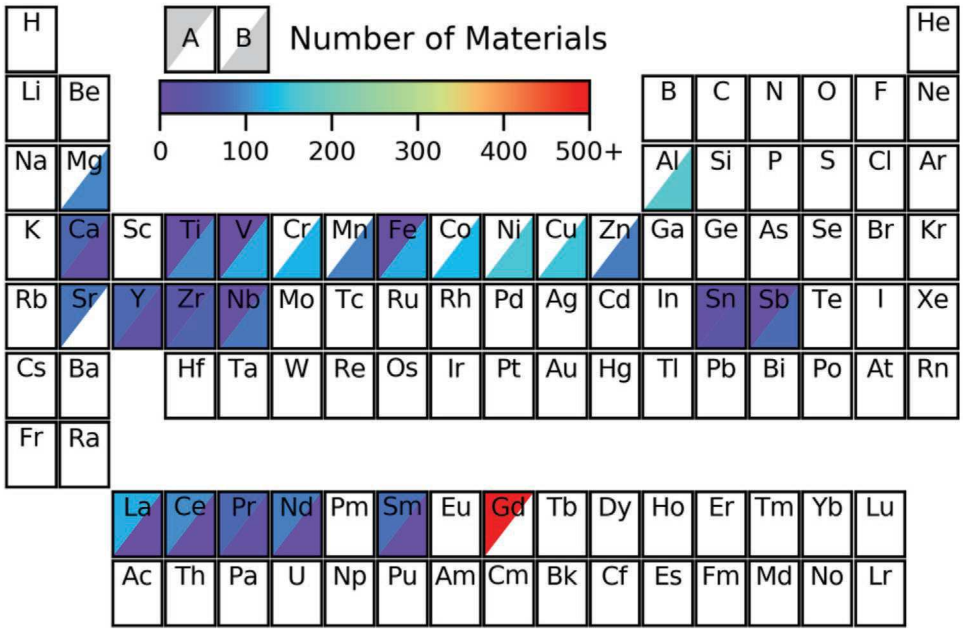

Figure 4. Periodic table plot of the 824 $Gd_2BB'O_6$, $GdA'B_2O_6$, and $GdA'BB'O_6$ perovskite compositions evaluated using high-throughput DFT calculations. A-site occupation is indicated by the color in the upper left corner of each element, whereas B-site occupation is indicated by the color in the lower right corner. Consistent with experiment, lanthanides most frequently occupy A-sites in our dataset, while transition metals most frequently occupy the B-sites. As indicated in the figure, all compositions investigated herein have Gd occupying the A-site.

2.2. Computational Scheme Used to Identify STCH Candidates

2.2.1. Composition Selection Using the Tolerance Factor τ

Experimental ABO_3 perovskites are more frequently observed with Gd^{3+} occupying the A-site than the B-site.[32] The Gd-containing perovskite oxides investigated herein were therefore limited to $Gd_2BB'O_6$, $GdA'B_2O_6$, and $GdA'BB'O_6$ compositions, where Gd only occupies the perovskite A-site. 4392 charge-balanced Gd-containing compositions were enumerated using combinations of the 24 elements determined to be commercially viable, nontoxic, nonradioactive, and therefore relevant for STCH (see the Supporting Information "Viable STCH Elements"). These 4392 compositions were first screened by their perovskite stabilities using τ.[33] τ classifies ABX_3 compositions as perovskite or nonperovskite using the Shannon radii[34] of the A, B, and X cations and the formal oxidation state of the A-site cation as inputs. Furthermore, τ can be extended to the $A_2BB'X_6$, $AA'BB'X_6$, etc. compositions by fractionally weighting the A- and B-site cation radii. Fractional weighting results in a 91% classification accuracy for $A_2BB'X_6$ compositions, only slightly lower than the 92% accuracy τ achieves for the ABO_3 single perovskites on which it was trained. τ predicts that 1325 of 4392 compositions evaluated herein are synthesizable as perovskites (e.g., $\tau_{prob} > 0.5$). For the present work, the STCH relevant properties for 824 of the 890 Gd-containing compositions that have $\tau_{prob} \geq 0.8$—and are therefore most likely to be stable as perovskites—were predicted using DFT. We were unable to predict structures for 66 of 890 compositions due to missing bond valence parameters for some cations (e.g., Ti^{2+}). **Figure 4** displays the frequency of A- and B-site occupation of all elements in the 824 Gd-containing compounds. Consistent with experimental perovskite oxides,[32] τ predicts that transition metals and metalloids most frequently occupy the B-sites, whereas alkali, alkaline earth and lanthanide elements most frequently occupy the A-sites.

2.2.2. Initial Structure Generation for DFT

BVM Initial Structure Prediction: Initial perovskite geometries for the 824 compositions optimized by DFT were generated using PySPuDS, a custom high-throughput python wrapper for the BVM-based SPuDS program.[35] For perovskites, the symmetry and magnitude of BO_6 octahedral tilting can be described using Glazer notation (e.g., $a^-b^+a^-$).[31] SPuDS predicts the magnitude of high-symmetry BO_6 octahedral tilting for 11 Glazer modes by minimizing the BVM Global Instability Index (*GII*), which is strongly correlated with the DFT energies of experimental ABO_3 perovskite oxide compositions.[36,37] SPuDS can therefore accurately estimate the magnitude of BO_6 octahedral tilting for a given phase relative to structures optimized using DFT. Additionally, we have previously shown that the DFT-optimized orthorhombic symmetry ($a^-b^+a^-$ Glazer mode) is the ground state perovskite structure predicted for ≈95% ABO_3 compositions examined.[38] To best capture the ground state properties of $Gd_2BB'O_6$, $GdA'B_2O_6$, and $GdA'BB'O_6$ perovskites, all initial structures for DFT optimization in the present investigation were generated by SPuDS in the monoclinic $P2_1/n$ (#14) space group ($a^-b^+a^-$ Glazer mode). For reference, an example $AA'BB'O_6$ structure generated in the $a^-b^+a^-$ Glazer mode is depicted in Figure 3B. The perovskite compositions with B-site alloying (e.g., $Gd_2BB'O_6$ and $GdA'BB'O_6$) were generated using rock salt site ordering, while the perovskite compositions with A-site alloying (e.g., $GdA'B_2O_6$ and $GdA'BB'O_6$) were ordered to minimize the Ewald sum over the four perovskite A-sites in the 20-atom unit cell of the $a^-b^+a^-$ Glazer mode.

Monte Carlo Site Displacements of High-Symmetry Structures: SPuDS generates perovskite structures that are stabilized by BO_6 tilting without the incurred expense of DFT geometry optimizations. This is vital to high-throughput computational investigations of STCH relevant properties, as previous computational studies of ABX_3 and $A_2BB'X_6$ perovskites (X = O, Cl, F, Br) have shown that the stabilities, oxygen vacancy enthalpies, and electronic properties (e.g., band gap and DOS m_e) of perovskites are highly sensitive to the BX_6 tilting phase and magnitude.[39–41] However, BO_6 tilting alone cannot capture all experimentally observed properties of perovskite oxides. For instance, off-site displacements of Ti within the TiO_6 octahedra result in the observed ferroelectricity of the perovskite oxides $PbTiO_3$ and $BaTiO_3$.[42] Because SPuDS generates high-symmetry Glazer tilt structures—which restricts B-sites to their high-symmetry positions within the BO_6 octahedra—when optimized in DFT these structures cannot capture the more subtle electronic effects observed in perovskite oxides with lower symmetry.[43] Therefore, we perturbed the site positions of structures predicted by SPuDS from their high-symmetry positions prior to DFT optimization using a modified MC rattling procedure.[44] MC rattling breaks crystal symmetries while maintaining physical interatomic distances, which allows DFT optimization to better capture the effects of symmetry-breaking on STCH relevant properties.

2.2.3. High-Throughput DFT Screening to Identify STCH Candidates

Stage 1: Materials Project-Compatible Geometry Optimization to Predict E_{Hull}: The 824 τ-stable Gd-containing perovskite structures—generated in the $a^-b^+a^-$ Glazer tilt and MC-rattled—were first screened by their DFT-predicted phase stabilities. Because all 824 of these perovskites contain Gd, which is a magnetic element, their magnetic ordering must be specified prior to DFT optimization. For a set of 252 binary compounds, Stevanovic et al. showed that the stabilization attributed to magnetic orderings other than high-spin ferromagnetic (FM), i.e., antiferromagnetic (AFM) or ferrimagnetic (FiM), is on the order of 10–20 meV/atom.[45] Likewise, we also found that the mean difference in DFT total energies between ABO_3 perovskites initialized as FM versus the lowest energy ABO_3 perovskite initialized in up to 20 unique AFM orderings was 7 meV/atom, although some outliers can exceed 100 meV/atom.[38] Because these reported differences are typically very small, the 824 structures optimized by DFT were initialized with FM ordering and evaluated by their stabilities relative to competing phases tabulated in the MP database. The energy of a material relative to the convex hull, E_{Hull}, quantifies its energy relative to the energies of its decomposition products. For the present work, the 385 perovskite oxides with DFT-computed, FM $E_{\mathrm{Hull}} \leq$ 60 meV/atom were magnetically sampled in Stage 2 of DFT screening. This E_{Hull} tolerance accommodates the reported error of ~30 meV/atom intrinsic to DFT-computed oxide formation energies[46] as well as the additional 0–20 meV/atom error that can, on average, be attributed to FM initialization in DFT.[38,45]

Stage 2: Self-Consistent Bulk Magnetic Sampling to Predict E_g and m_e^*: Whereas DFT stability predictions are relatively insensitive to magnetic ordering—particularly when stability prediction errors are incorporated into the screening scheme, as we have done using the E_{Hull} tolerance—electronic property predictions are considerably more susceptible to the spin configuration. For instance, Malyi et al. showed that DFT optimizations of $YTiO_3$ and $LaTiO_3$ perovskite oxides that did not correctly consider magnetic ordering resulted in false metal predictions ($E_{\mathrm{g}} = 0$) for these semiconductors.[47] High-throughput computational schemes in which materials are indiscriminately initialized high-spin, high-symmetry FM and optimized in DFT are likely insufficient to reliably predict metallic/non-metallic behavior. This shortcoming is particularly detrimental for STCH candidate discovery, as the STCH-relevant m_e^* are generally computed for semiconductors and insulators ($E_{\mathrm{g}} > 0$) using DFT. To mitigate inaccurate electronic property predictions in Gd-containing perovskites, geometry optimizations followed by self-consistent field (SCF) DFT calculations in up to 20 unique initial magnetic orderings were performed for each of the 385 geometry-optimized candidate structures. Magnetic sampling was performed using pymatgen's MagneticStructureEnumerator module, which computes all symmetrically unique magnetic orderings for a structure's elements and site positions. Sampling introduces initial spin disorder that can widen artificially small E_{g} attributable to high-symmetry spin initializations. Following magnetic sampling, 311 of 385 compositions were computed to have $E_{\mathrm{g}} > 0$, and therefore a nonzero m_e^*. These 311 perovskites were passed to the subsequent stage of DFT evaluation of oxygen vacancy formation energies, of which we successfully completed calculations for 231 of the 311 materials. For the remaining 80 compositions, convergence issues resulted in either unphysical oxygen vacancies, i.e., $\Delta H_{\mathrm{Ovac}} < 0$ or $\Delta H_{\mathrm{Ovac}} \gg 10$ eV, or unconverged calculations for which ΔH_{Ovac} could not be computed. As a result, and although a number of these materials could be competent redox mediators, these 80 compositions were excluded from further analysis.

Stage 3: Defect Cell Oxygen Vacancy Calculations to Estimate ΔH_{TR}: The ΔH_{TR} of STCH redox mediators dictates many STCH properties, from hydrogen production capacity to long-term cyclability.[5] Thermal reduction of STCH materials in two-step processes typically follows one of two reduction mechanisms, either: 1) a complete or partial phase change, such as the complete reduction of ZnO to elemental Zn,[48] or 2) an off-stoichiometry mechanism during which oxygen vacancies form but the phase is preserved, such as the partial reduction of the $Sr_xLa_{1-x}Mn_yAl_{1-y}O_3$ (SLMA) perovskites.[11,13,14] ΔH_{TR} is typically estimated using DFT-computed oxygen vacancy formation enthalpies at $T = 0$ K, ΔH_{Ovac} (eV). ΔH_{TR} of a redox mediator can therefore be estimated by DFT using Equation (3)

$$\Delta H_{TR} \approx \Delta H_{\mathrm{Ovac}} = E_{\mathrm{tot}}^{\mathrm{defect}} - E_{\mathrm{tot}}^{\mathrm{Host}} + \mu_{\mathrm{O}} \tag{3}$$

where $E_{\mathrm{tot}}^{\mathrm{Host}}$ is the DFT total energy of the defect-free (Host) oxide, $E_{\mathrm{tot}}^{\mathrm{defect}}$ is the DFT total energy of the reduced/defective oxide containing a single oxygen vacancy, and μ_{O} is the chemical potential of oxygen at $T = 0$ K. Herein, we define $\mu_{\mathrm{O}} = -4.948$ eV/atom, which is the lowest energy O_2 entry tabulated in the MP (mp-12957). We also assume that the 231 Gd-containing perovskite oxide candidates in our screening are reduced via the off-stoichiometry mechanism, which is most frequently observed in STCH active perovskite oxides.[11,12,26] ΔH_{TR} was

ADVANCED FUNCTIONAL MATERIALS
www.afm-journal.de

Table 1. Computed E_{Hull}, m_e^*, E_g, and $\overline{\Delta H}_{Ovac}$ for eight STCH active perovskite compositions identified by computational screening. The STCH activities of $SrLaMnAlO_6$, Sr_2TiMnO_6, and Ca_2TiMnO_6 were previously demonstrated. Materials are ordered by increasing average oxygen vacancy enthalpy. The DFT predicted structures for $SrGdMnAlO_6$, $GdLaCoFeO_6$, and $GdLaMnNiO_6$ are shown in Figures S4 and S5 (Supporting Information).

Compound	E_{Hull} [meV/atom]	m_e^*	E_g [eV]	$\overline{\Delta H}_{Ovac}$ [eV]	First discovered by this framework	Other references
$SrGdMnAlO_6$	33.4	2.54	1.09	1.95	Yes	Bare et al.[54]
$SrLaMnAlO_6$	77.0	3.27	1.50	2.10	No	McDaniel et al.a)[11]
Sr_2TiMnO_6	7.8	7.31	1.31	2.23	No	Qian et al.a)[57]
Ca_2TiMnO_6	5.9	9.46	1.71	2.38	No	Qian et al.a)[58]
$GdLaCoFeO_6$	0.0	8.52	1.01	2.77	Yes	Park et al.[52]
La_2MnNiO_6	48.0	4.04	1.61	3.13	Yes	Morelock et al.[53]
$GdLaMnNiO_6$	58.8	2.36	1.35	3.33	Yes	Morelock et al.[53]
Nd_2MnNiO_6	0.6	2.63	1.49	3.67	Yes	Morelock et al.[53]

a)References to experimental demonstrations of STCH activity for Mn-containing known STCH redox mediators that this work rediscovered.

therefore estimated using DFT charge-neutral oxygen vacancy defect calculations, enforcing an oxygen vacancy defect concentration limit of $C_d < 0.1$ to avoid spurious self-interactions with periodic images. Distortions that lower the symmetry relative to the nominal cubic perovskite, such as BO_6 tilting and MC-rattling prior to DFT optimization, can lead to variable local oxygen coordination environments within the theoretical structures investigated herein. These unique oxygen environments result in distributions of ΔH_{Ovac}; accordingly, defect calculations were performed for all symmetrically unique oxygen sites present in the bulk perovskite lattices. Symmetrically unique oxygen sites were determined using pymatgen's PointGroupAnalyzer module.

Our screening approach prioritizes Gd-containing compositions with 1.95 eV ≤ ΔH_{Ovac} ≤ 3.95 eV. We preferentially screen for compositions with $\Delta H_{Ovac} \leq 3.95$ eV because CeO_2 has $\Delta H_{Ovac} = 3.95$ eV computed within our high-throughput framework, and CeO_2 only exhibits its exceptional H_2 production capacities near the upper limit of the practical STCH temperature range ($T_{red} \geq 1500$ °C).[9] We evaluated compositions that have computed ΔH_{Ovac} within −2 eV of CeO_2 ($\Delta H_{Ovac} \geq 1.95$ eV), which includes compositions with ΔH_{Ovac} greater than the standard state formation enthalpy of steam, $\Delta H_{H_2O(g)} \approx 2.5$ eV.[49] STCH activity under high-pressure steam conditions can be observed for redox mediators with $\Delta H_{TR} \approx \Delta H_{Ovac} < 2.5$ eV such as hercynite ($FeAl_2O_4$), whereby H_2 production is driven by the chemical potential difference between the reduced mediator and reactor steam conditions.[50] Cycles that change the chemical potential difference incur additional energetic costs, however, and are therefore suboptimal.[51] Despite this, we consider some compositions with $\Delta H_{Ovac} < 2.5$ eV, consistent with previous DFT investigations,[16,22] as these perovskites could feasibly demonstrate STCH activity under certain reactor conditions.

2.3. Data Set Statistics and STCH Candidates

2.3.1. STCH Active Materials Identified by Computational Screening

Table 1 lists the DFT-computed properties of the Gd-containing compositions identified by our computational approach that were referred to experimental collaborators, who synthesized them as perovskites and demonstrated their STCH activity.[52–54] We chose the compositions $GdLaCoFeO_6$, $GdLaMnNiO_6$, and $SrGdMnAlO_6$ for initial experimental studies because similar compositions have documented perovskite synthesis procedures that could be easily modified by our experimental collaborators,[11,55,56] and they exhibit E_{Hull} and $\overline{\Delta H}_{Ovac}$ values that span the full range of screening criteria used in this study (0 meV/atom ≤ E_{Hull} ≤ 60 meV/atom and 1.95 eV/atom ≤ $\overline{\Delta H}_{Ovac}$ ≤ 3.95 eV/atom). $GdLaCoFeO_6$ (GLCF) has $E_{Hull} = 0$ eV/atom and $\overline{\Delta H}_{Ovac}$ near the middle of our range ($\overline{\Delta H}_{Ovac}$ = 2.77 eV/atom). $SrGdMnAlO_6$ (SGMA) has E_{Hull} = 33.4 eV/atom, or near the middle of our stability range, and a $\overline{\Delta H}_{Ovac}$ at the lower bound of our range ($\overline{\Delta H}_{Ovac}$ = 1.95 eV/atom). Finally, E_{Hull} and $\overline{\Delta H}_{Ovac}$ of $GdLaMnNiO_6$ (GLMN) both approach the upper end of our ranges (58.8 and 3.33 eV/atom, respectively).

To further validate our high-throughput computational workflow we also evaluated Mn-containing perovskites, including three known STCH-active perovskite manganates, as they have been extensively investigated as STCH redox mediators. Application of our workflow to Mn-containing multinary perovskites (compositions $A_2MnB'O_6$, $AA'Mn_2O_6$, and $AA'MnB'O_6$, see the Supporting Information "Investigation of Mn-containing Perovskite Oxides") rediscovers the known STCH-active perovskites $SrLaMnAlO_6$, Sr_2TiMnO_6, and Ca_2TiMnO_6 as promising STCH candidates. The DFT properties of these materials computed using our workflow are also listed in Table 1. This work also identified the perovskite manganates La_2MnNiO_6 and Nd_2MnNiO_6 as promising STCH candidates, which to our knowledge had not yet been reported as STCH-active. We also referred these materials to our experimental collaborators who successfully synthesized and demonstrated them as STCH active perovskites.[53] The identification of STCH competent Mn-containing redox mediators using our scheme further illustrates the generalizability of the empirical approaches used herein.

The broad $\overline{\Delta H}_{Ovac}$ range of 1.7 eV, as well as the observed conditions of $E_g > 0$ and $E_{Hull} < 60$ meV/atom for STCH active materials in Table 1 (apart from SLMA), justify our MP compatible screening criteria. SGMA was discovered using our scheme and has a $\overline{\Delta H}_{Ovac}$ of 1.95 eV, representing the lower ΔH_{Ovac} boundary (1.95 eV) used to identify STCH redox mediator candidates in the present investigation. The SGMA composition

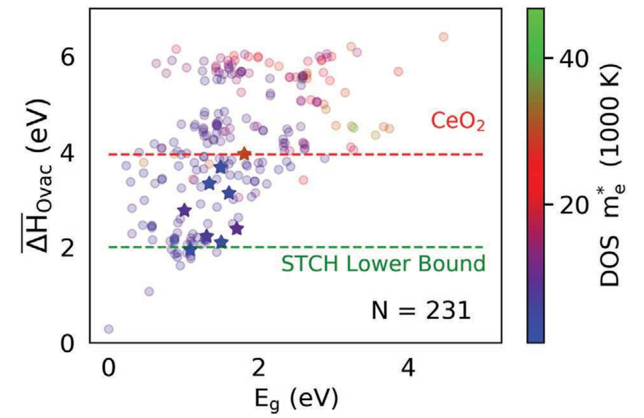

Figure 5. STCH relevant properties for the 231 Gd compounds evaluated in Stage 3 of our screening scheme. The stars indicate CeO_2 and the eight experimentally verified water splitting materials listed in Table 1. We identified 83 of 231 compounds with $\overline{\Delta H}_{Ovac}$ within the estimated STCH active range (1.95 eV $\leq \overline{\Delta H}_{Ovac} \leq$ 3.95 eV). Generally, E_g and $\overline{\Delta H}_{Ovac}$ increase with increasing m_e^*, and most of the compounds with the largest m_e^* are outside of the STCH active range of $\overline{\Delta H}_{Ovac}$.

$Sr_{0.4}Gd_{0.6}Mn_{0.6}Al_{0.4}O_3$ exhibits hydrogen production capacities of 141, 162, and 171 μmol g^{-1} over three consecutive redox cycles under 40% volume H_2O conditions and with reduction and oxidation temperatures of T_{TR} = 1350 °C and T_{WS} = 850 °C, respectively.[54] Qian et al. identified the perovskite oxide Ca_2TiMnO_6 (CTM55) and demonstrated its exceptional STCH yield of 10.0 mL g^{-1} at T_{TR} = 1350 °C and T_{WS} = 1150 °C with a cycle time of 1.5 h.[58] Our computational approach predicts the $\overline{\Delta H}_{Ovac}$ of this material to be 2.38 eV, well within the STCH active range, and predicts a relatively large, favorable contribution from $\Delta S_{TR,elec}$ attributed to its relatively high m_e^* of 9.46. Our computational approach predicted similar properties and water splitting behavior for the perovskite oxide Sr_2TiMnO_6 (STM55) identified by Qian et al.[57]

GLCF was identified by our computational approach and exhibited hydrogen production capacities of 101 and 141 μmol g^{-1} over consecutive redox cycles.[52] GLCF also has improved STCH cyclability relative to the similar perovskite oxides $La_{0.6}Sr_{0.4}Co_{0.2}Fe_{0.8}O_3$ and $LaFe_{0.75}Co_{0.25}O_3$, which degrade during redox cycling. This behavior was explained by GLCF's broad ΔH_{Ovac} range computed using our computational scheme relative to the previously reported perovskite $LaCo_{0.5}Fe_{0.5}O_3$[59] (L2CF); vacancies with larger ΔH_{Ovac} are less likely to form at water splitting temperatures, and thus preserve the perovskite lattice during redox cycling. The perovskite oxide compositions GLMN, $LaMn_{0.5}Ni_{0.5}O_3$ (L2MN), and $NdMn_{0.5}Ni_{0.5}O_3$ (Nd2MN) were first computationally predicted using our scheme and subsequently characterized for their STCH activity by Morelock et al.[53] Relative to GLCF, GLMN, and L2MN exhibited enhanced hydrogen production capacities with H_2 present in a 1:1333 ratio to steam (16 μmol g^{-1} vs 36 μmol g^{-1} and 34 μmol g^{-1}). This novel STCH behavior was rationalized by GLMN and L2MN's average oxygen vacancy enthalpies $\overline{\Delta H}_{Ovac}$, as these materials possess $\overline{\Delta H}_{Ovac}$ (3.33 and 3.13 eV) that are closer to the $\overline{\Delta H}_{Ovac}$ of the high-conversion redox mediator CeO_2 (3.95 eV) than the $\overline{\Delta H}_{Ovac}$ of GLCF (2.77 eV). All of Nd2MN's unique oxygen sites have ΔH_{Ovac} > 3.40 eV, which approach the upper boundary of our screening of ΔH_{Ovac} = 3.95 eV. Like CeO_2, the corresponding large ΔH_{TR} of Nd2MN predicted from $\overline{\Delta H}_{Ovac}$ results in significantly decreased STCH production relative to L2MN at T_{TR}= 1350 °C when H_2 is not present in steam.

2.3.2. Computationally Identified STCH Candidate Materials

Of the 231 compounds evaluated in Stage 3 of our screening, 83 have 1.95 eV $\leq \overline{\Delta H}_{Ovac} \leq$ 3.95 eV. Additional STCH relevant properties for the 83 candidate materials are listed in Gd_Multinary_Perovsktie_Oxide_STCH_Candidates.csv. The most promising STCH candidates should have m_e^* comparable to that of CeO_2 (m_e^* = 30.71) and $\overline{\Delta H}_{Ovac}$ in the STCH active range; however, we find that as m_e^* increases, E_g and $\overline{\Delta H}_{Ovac}$ generally increase as well, which can result in $\overline{\Delta H}_{Ovac}$ outside the STCH active range (**Figure 5**). The increase in $\overline{\Delta H}_{Ovac}$ with increasing E_g is consistent with the results reported by Deml et al., who used this correlation to predict the oxygen vacancy formation enthalpies of 45 binary and ternary oxides.[60] We find that compounds with m_e^* > 20 possess $\overline{\Delta H}_{Ovac}$ > 3.95 eV/atom, with a few notable exceptions. For example, compounds with Ce on the A-site, namely, $CeGdCoNiO_6$, $CeGdMnNiO_6$, and $CeGdCoFeO_6$ have the largest m_e^* (38.30, 29.30, and 32.05, respectively) of all compounds with $\overline{\Delta H}_{Ovac}$ in the STCH active range (3.44, 3.80, and 3.95, respectively), and are therefore predicted to be excellent candidates for STCH. Likewise, $GdYMn_2O_6$ is a promising STCH candidate, with m_e^* = 31.88, E_{Hull} = 7 meV/atom, and $\overline{\Delta H}_{Ovac}$ = 3.77 eV. However, the bandgap of $GdYMn_2O_6$ (E_g = 0.47 eV) is small, which may restrict temperature-dependent changes in the Fermi level under STCH operating conditions and thus the magnitude of $\Delta S_{TR,elec.}$ $GdSmAlFeO_6$ is another promising STCH candidate, with m_e^* = 21.85, E_{Hull} = 24.77 meV/atom, and $\overline{\Delta H}_{Ovac}$ = 3.38 eV. However, the computed bandgap of $GdSmAlFeO_6$ (E_g = 2.60 eV) is 0.8 eV larger than that of CeO_2, which could inhibit electron promotion to states near the CBM at STCH reduction temperatures and thus limit $\Delta S_{TR,elec}$.

Although few materials possess both large m_e^* and $\overline{\Delta H}_{Ovac}$ in the STCH active range, we find 78 potential STCH candidates with low to intermediate m_e^* (1.0 $\leq m_e^* \leq$ 20.0) and 1.95 eV $\leq \overline{\Delta H}_{Ovac} \leq$ 3.95 eV. These candidates include the experimentally demonstrated water-splitting materials in Table 1, which are displayed as stars and colored by m_e^* in Figure 5. The majority of STCH candidates contain a 3d transition metal (Cr, Mn, Fe, Co, and/or Ni) and/or Al, Mg, or Sb on the B-sites, and a lanthanide (La, Y, Pr, Nd, Sm, or Gd) or Ca/Sr mixed with Gd on the A-site (**Figure 6**). For compounds with fixed B/B′ elements, we find that lanthanide/Gd mixing on the A-site results in higher $\overline{\Delta H}_{Ovac}$ compared with Sr/Gd or Ca/Gd mixing on the A-site, and that Ca generally has a slightly larger $\overline{\Delta H}_{Ovac}$ compared with Sr (see Figure S6, Supporting Information). As a result, when B and B′ elements are fixed between compositions the most promising STCH candidates have either lanthanides or Sr/Ca occupying the A-site with Gd, but rarely both (**Table 2**). One notable exception is the Gd-A′-Al-Mn-O chemical space, in which the Sr and Ca containing compounds have $\overline{\Delta H}_{Ovac}$

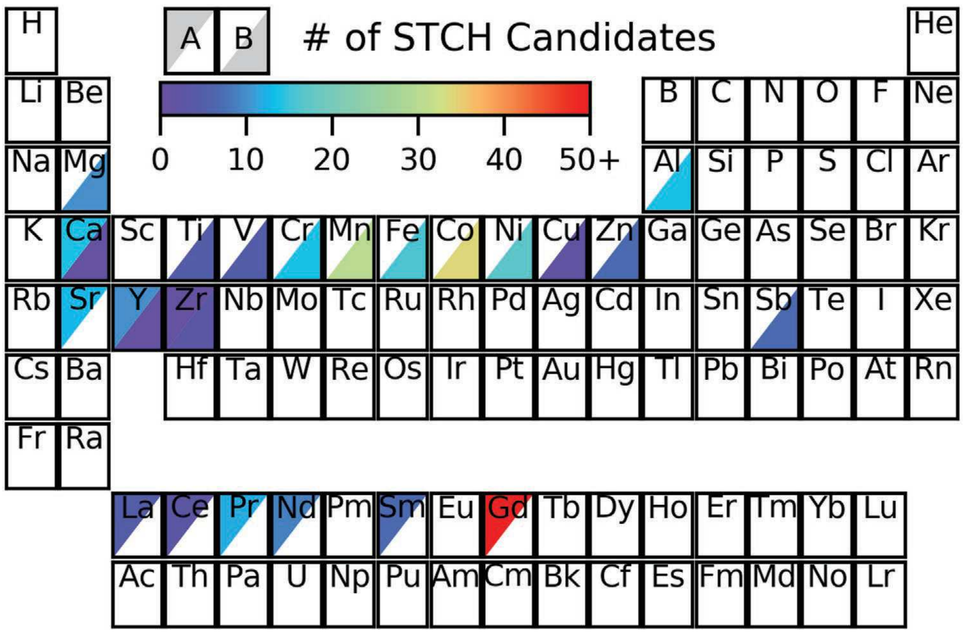

Figure 6. Periodic table plot of the 83 $Gd_2BB'O_6$, $GdA'B_2O_6$, and $GdA'BB'O_6$ STCH candidate perovskite compositions. A-site occupation is indicated by the color in the upper left corner of each element, whereas B-site occupation is indicated by the color in the lower right corner. The majority of STCH candidates contain a 3d transition metal (Cr, Mn, Fe, Co, and/or Ni) and/or Al, Mg, or Sb on the B-sites, and a lanthanide (La, Y, Pr, Nd, Sm, or Gd) and/or Ca/Sr mixed with Gd on the A-site.

approaching the lower end of the STCH active range (1.95 and 2.62 eV, respectively) and the lanthanide elements Y, Pr, Nd, Sm, and Gd have $\overline{\Delta H}_{\text{Ovac}}$ approaching the upper bound of the STCH active range (3.86, 3.64, 3.90, 3.90, and 3.62 eV, respectively). Substitution of Sr, Ca, and lanthanides on A-sites of perovskites within the Gd-A′-Al-Mn-O chemical space should therefore result in a class of highly tunable STCH materials that exhibit a broad range of $\overline{\Delta H}_{\text{Ovac}}$.

Table 2. Ranges of STCH relevant properties grouped by unique B/B′ sites for 65 of the 83 $GdA'BB'O_6$ STCH candidates with A′ = Ca, Sr, or a lanthanide. The m_e^* of Ce-containing STCH candidates that are outliers with respect to other lanthanide elements with fixed B/B′ elements are reported in parentheses.

B	B′	A′ (Alk)	A′ (Ln)	E_g range [eV]	$\overline{\Delta H}_{\text{Ovac}}$ range [eV]	m_e^* range
Al	Mn	Ca, Sr	Y, Pr, Nd, Sm, Gd	1.09–1.73	1.95–3.90	2.54–5.97
Co	Co	–	Y, La, Nd	0.92–1.10	2.05–2.30	7.50–9.82
Co	Fe	–	Y, La, Ce, Pr, Nd, Gd	0.88–1.61	2.49–3.95	3.20–8.52 (32.05)
Al	Co	–	Y, La, Pr, Gd	0.96–2.02	2.59–3.63	4.84–6.42
Cr	Ni	–	Pr, Nd, Sm	0.58–0.58	2.40–2.45	3.46–3.6
Mn	Ni	–	Y, La, Ce, Pr, Gd	1.34–1.73	3.33–3.74	2.36–3.58 (29.30)
Co	Mg	–	Y, La, Pr, Nd, Sm, Gd	1.12–1.31	2.05–2.28	3.86–7.72
Co	Ni	–	Y, Ce, Nd, Gd	0.29–1.12	1.95–3.42	2.72–3.76 (28.30)
Mg	Mn	–	Y, Pr	1.95–1.95	3.38–3.38	3.52–3.79
Co	Cr	–	Nd, Sm, Gd	0.62–1.54	3.34–3.85	5.09–6.75
Cr	Zn	–	Pr, Nd, Sm, Gd	0.82–1.10	2.12–2.19	3.54–3.82
Mn	Mn	–	Y, Sm	0.23–0.47	3.71–3.77	1.77–31.89
Cu	Fe	–	Y, Pr	0.31–0.31	2.28–2.82	4.94–5.94
Fe	Sb	Ca, Sr	–	1.83–2.05	3.73–3.78	5.43–5.58
Cr	Mn	Ca, Sr	–	1.23–1.23	2.90–3.26	3.61–3.86
Fe	Ti	Ca, Sr	–	1.85–2.11	3.32–3.70	2.98–3.41
Ni	Sb	Ca, Sr	–	2.38–2.89	3.79–3.86	4.12–4.76
Mn	Ti	Ca, Sr	–	0.48–0.71	2.98–3.42	1.88–2.06
Sb	Zn	Ca, Sr	–	2.27–2.43	3.63–3.69	1.38–1.43
Mn	Zr	Ca, Sr	–	0.47–0.94	3.55–3.70	1.12–2.17

Chemical spaces with at least two compounds in the STCH active range are grouped by B/B′ site and listed in Table 2. In addition to the Gd-A′-Al-Mn-O chemical space, we identified 12 unique B/B′ combinations with Gd-lanthanide mixing on the A-site and seven unique B/B′ combinations with Gd-Ca/Sr mixing on the A-site which contain compositions in the STCH active range. The B/B′ combinations Cr/Ni, Mn/Mn, and Cu/Fe have small computed bandgaps ($E_g < 0.6$ eV), whereas the B/B′ combinations Ni/Sb and Sb/Zn have large computed bandgaps ($E_g > 2.2$ eV). The properties of these B/B′ combinations are relatively unaffected by the identity of the A-site cation, which could limit electronic property (i.e., E_g and m_e^*) tuning within these chemical spaces. Additionally, the B-site combinations Co/Co, Cr/Ni, Co/Mg, and Cr/Zn have compositions with $\overline{\Delta H}_{Ovac} < 2.77$, which is the $\overline{\Delta H}_{Ovac}$ computed for GLCF. GLCF has poor STCH performance under high steam-to-hydrogen ratios, which are relevant conditions for industrial-scale STCH production.[53] We anticipate that perovskite oxides with these B-site combinations will therefore have insufficient ΔH_{TR} to underly grid-scale STCH technologies. The remaining B-site combinations (Co/Fe, Al/Co, Mn/Ni, Co/Ni, Mg/Mn, Co/Cr, Fe/Sb, Cr/Mn, Fe/Ti, Mn/Ti, and Mn/Zr) are predicted to contain industrially relevant STCH candidate perovskite oxides and could provide exceptional STCH materials with further compositional tuning.

3. Conclusions

We report a high-throughput framework to evaluate complex multinary perovskite oxide spaces for their STCH applications. We focus this investigation on the relatively unstudied Gd-containing perovskite oxides (compositions $Gd_2BB'O_6$, $GdA'B_2O_6$, and $GdA'BB'O_6$) because $GdBO_3$ perovskites have large predicted m_e^*, and are therefore likely to possess large ΔS_{TR} under STCH conditions. Our theoretical materials screening framework leverages ab initio and empirical methods to characterize the stability, structure, and STCH relevant properties of these materials (i.e., E_g, m_e^*, and $\overline{\Delta H}_{Ovac}$). From a candidate space of 4392 possible compositions, we identified 83 Gd-containing STCH candidates, three of which have been synthesized and demonstrated experimental STCH activity by our experimental collaborators. By extending this framework to other compositions of interest to the STCH community, i.e., the Mn-containing perovskite oxides, we rediscovered three previously known STCH redox mediators and discovered two novel STCH-active perovskites, further validating our screening approach. Ultimately, we report several STCH candidate redox mediators in the multinary perovskite oxide space and an effective high-throughput approach to screen vast alloyed compositional spaces for solar thermochemical applications.

4. Experimental Section

DOS Electron Effective Mass Calculations: Cation contributions to the DOS electron effective mass (m_e^*) were calculated from the DFT orbital-projected DOS computed for non–defect host structures. Energy densities contributing to cation-specific DOS effective masses were multiplied by their temperature-dependent Boltzmann weighting

$$w_{E_i} = e^{(E_i - E_{CBM})/kT} \tag{4}$$

where w_{E_i} is the weighting associated with a given eigenvalue i, E_i, E_{CBM} is the orbital-projected conduction band minimum as determined from the vasprun.xml output of the Vienna Ab Initio Simulation Package, VASP, and kT is Boltzmann's constant multiplied by the temperature of interest (T = 1000 K for the present work). The orbital projected DOS effective mass of cation j, m_e^*, is calculated as the following summation

$$m_e^* = \sum_i w_{E_i} \cdot DOS(E_i) \cdot dE \tag{5}$$

where $DOS(E_i)$ is the density of electronic states at the energy level E_i above E_{CBM}, and dE is the energy difference between eigenvalues i and i+1.

Structure Generation and Optimization: All Gd-containing compositions with $\tau_{prob} \geq 0.8$ were input to SPuDS (DOS version > 2.20.08.06) and generated in the $a^-b^+a^-$ Glazer octahedral tilt system using a custom python wrapper; this python wrapper is publicly available for download at https://github.com/zaba1157/PySPuDS. SPuDS enforces symmetric BO_6 octahedra and the B-site occupation of high-symmetry Wyckoff positions. MC rattling was therefore performed to break these symmetry constraints prior to DFT optimization. Magnetic effects on the stabilities and electronic properties of theoretical perovskites were explicitly considered by first performing two consecutive spin-polarized relaxations initialized in a high-spin ferromagnetic configuration, with species-specific initial magnetic moments dictated by the default MP spin parameters. Magnetic sampling of these computed structures was performed for up to 20 different magnetic symmetries using pymatgen's MagneticStructureEnumerator. Finally, the internal coordinates of the DFT structures—with lattice vectors and initial magnetic moments fixed from previous optimizations—were optimized such that total energies were converged to within 10^{-6} eV and forces were converged to within 0.01 eV Å^{-1}. In this manner, the effects of spin configuration on the electronic DOS were explicitly captured. All geometry optimizations were performed without symmetry constraints on the optimized wavefunction.

GGA+U DFT calculations were performed using the Vienna Ab-initio Simulation Program (VASP 5.4.1)[61–63] with the Perdew–Burke–Ernzerhof (PBE)[64] exchange-correlation functional and periodic boundary conditions using projector augmented wave (PAW) pseudopotentials.[65,66] All calculations are compatible with the MP database, which tabulates the structures and energies of inorganic materials computed at the PBE (GGA+U) level of theory. The electronic wave functions were expanded in a plane wave basis set with an energy cutoff of 520 eV. The Brillouin zones were sampled during geometry optimizations using the Monkhorst–Pack algorithm to automatically generate a Γ-point centered k-point mesh with a grid density of at least 1000/(atoms/unit cell). The specific pseudopotentials used are consistent with pymatgen's MPRelaxSet, which is the default relaxation parameter set for the MP. Hubbard U parameters for the elements Mn, Fe, Co, Cr, Mo, W, V, and Ni were taken from the pymatgen[30] python package's MPRelaxSet, which tabulates U parameters calibrated using the approach described by Wang et al.[67] Energies above the convex hull, E_{Hull}, included MP-specific corrections as described by pymatgen's MP Compatibility Settings. These include oxide-specific corrections based on the structure type (i.e., oxide, peroxide, superoxide, or ozonide). As discussed in https://docs.materialsproject.org/methodology/total-energies/, the coordination environments of oxygen anions present in these materials determine their structure type classifications. E_{Hull} of DFT optimized $Gd_2BB'O_6$, $GdA'B_2O_6$, and $GdA'BB'O_6$ structures in this study's data set were calculated relative to their lowest enthalpy decomposition products as tabulated in the MP.

Supporting Information

Supporting Information is available from the Wiley Online Library or from the author.

Acknowledgements

Z.B. and R.M. contributed equally to this work. The authors would like to thank their experimental collaborators, A. H. McDaniel, A. W. Weimer, E. N. Coker, J. T. Tran, J. E. Park, A. Ambrosini, J. A. Trindell, and M. A. Rodriguez for synthesizing and characterizing the candidate materials. The authors also thank S.L. Millican for helpful discussions related to candidate materials selection. Z.B. generated the computational data, workflow scheme, STCH candidate materials plots, and wrote the manuscript. R.M. created the MP effective mass plot, substitution matrix plot, and wrote the manuscript. C.M. supervised the project and calculations and edited the manuscript. This work was supported by the U.S. Department of Energy (DOE), Office of Energy Efficiency and Renewable Energy (EERE), Hydrogen and Fuel Cell Technologies Office (HFTO), and specifically the HydroGEN Advanced Water Splitting Materials Consortium, established as part of the Energy Materials Network under this same office (Award No. DE-EE0008088). C.M., Z.B., and R.M. also acknowledge support from the National Science Foundation, Award Nos. NSF CHEM-1800592 and CBET-2016225. The views expressed in this article do not necessarily represent the views of the U.S. Department of Energy or the U.S. Government. R.M. would also like to acknowledge support from the University of Colorado-Boulder's Graduate Assistance in Areas of National Need, GAANN, Materials for Energy Conversion and Sustainability grant, Award No. P200A180012.

Conflict of Interest

The authors declare no conflict of interest.

Data Availability Statement

The data that support the findings of this study are available in the supplementary material of this article.

Keywords

concentrated solar energy, density functional theory, hydrogen, perovskite, thermochemical water splitting

Received: January 6, 2022
Revised: February 17, 2022
Published online: March 20, 2022

[1] A. Steinfeld, *Sol. Energy* **2005**, *78*, 603.
[2] G. Centi, S. Perathoner, *ChemSusChem* **2010**, *3*, 195.
[3] C. N. R. Rao, S. Dey, *Proc. Natl. Acad. Sci. USA* **2017**, *114*, 13385.
[4] B. Xu, Y. Bhawe, M. E. Davis, *Proc. Natl. Acad. Sci. USA* **2012**, *109*, 9260.
[5] C. L. Muhich, B. D. Ehrhart, I. Al-Shankiti, B. J. Ward, C. B. Musgrave, A. W. Weimer, *Wiley Interdiscip. Rev. Energy Environ.* **2016**, *5*, 261.
[6] N. P. Siegel, J. E. Miller, I. Ermanoski, R. B. Diver, E. B. Stechel, *Ind. Eng. Chem. Res.* **2013**, *52*, 3276.
[7] J. E. Miller, A. H. McDaniel, M. D. Allendorf, *Adv. Energy Mater.* **2014**, *4*, 1300469.
[8] B. Bulfin, J. Vieten, C. Agrafiotis, M. Roeb, C. Sattler, *J. Mater. Chem. A* **2017**, *5*, 18951.
[9] S. Abanades, G. Flamant, *Sol. Energy* **2006**, *80*, 1611.
[10] H. Kaneko, H. Ishihara, S. Taku, Y. Naganuma, N. Hasegawa, Y. Tamaura, *J. Mater. Sci.* **2008**, *43*, 3153.
[11] A. H. McDaniel, A. Ambrosini, E. N. Coker, J. E. Miller, W. C. Chueh, R. O'Hayre, J. Tong, *Energy Proc.* **2014**, *49*, 2009.
[12] D. R. Barcellos, M. D. Sanders, J. Tong, A. H. McDaniel, R. P. O'Hayre, *Energy Environ. Sci.* **2018**, *11*, 3256.
[13] J. R. Scheffe, D. Weibel, A. Steinfeld, *Energy Fuels* **2013**, *27*, 4250.
[14] M. Ezbiri, M. Takacs, D. Theiler, R. Michalsky, A. Steinfeld, *J. Mater. Chem. A* **2017**, *5*, 4172.
[15] T. Nakamura, *Sol. Energy* **1977**, *19*, 467.
[16] A. M. Deml, V. Stevanović, A. M. Holder, M. Sanders, R. O'Hayre, C. B. Musgrave, *Chem. Mater.* **2014**, *26*, 6595.
[17] J. Vieten, B. Bulfin, P. Huck, M. Horton, D. Guban, L. Zhu, Y. Lu, K. A. Persson, M. Roeb, C. Sattler, *Energy Environ. Sci.* **2019**, *12*, 1369.
[18] M. Kubicek, A. H. Bork, J. L. M. Rupp, *J. Mater. Chem. A* **2017**, *5*, 11983.
[19] B. Meredig, C. Wolverton, *Phys. Rev. B: Condens. Matter* **2009**, *80*, 245119.
[20] S. S. Naghavi, A. A. Emery, H. A. Hansen, F. Zhou, V. Ozolins, C. Wolverton, *Nat. Commun.* **2017**, *8*, 285.
[21] C. B. Gopal, A. van de Walle, *Phys. Rev. B: Condens. Matter* **2012**, *86*, 134117.
[22] S. S. Naghavi, J. He, C. Wolverton, *ACS Appl. Mater. Interfaces* **2020**, *12*, 21521.
[23] S. Lany, *J. Chem. Phys.* **2018**, *148*, 071101.
[24] A. A. Emery, C. Wolverton, *Sci. Data* **2017**, *4*, 170153.
[25] G. Sai Gautam, E. B. Stechel, E. A. Carter, *Chem. Mater.* **2020**, *32*, 9964.
[26] D. R. Barcellos, F. G. Coury, A. Emery, M. Sanders, J. Tong, A. McDaniel, C. Wolverton, M. Kaufman, R. O'Hayre, *Inorg. Chem.* **2019**, *58*, 7705.
[27] C.-K. Yang, Y. Yamazaki, A. Aydin, S. M. Haile, *J. Mater. Chem. A* **2014**, *2*, 13612.
[28] S. Dey, B. S. Naidu, C. N. R. Rao, *Chemistry* **2015**, *21*, 7077.
[29] A. Jain, S. P. Ong, G. Hautier, W. Chen, W. D. Richards, S. Dacek, S. Cholia, D. Gunter, D. Skinner, G. Ceder, K. A. Persson, *APL Mater.* **2013**, *1*, 011002.
[30] S. P. Ong, W. D. Richards, A. Jain, G. Hautier, M. Kocher, S. Cholia, D. Gunter, V. L. Chevrier, K. A. Persson, G. Ceder, *Comput. Mater. Sci.* **2013**, *68*, 314.
[31] A. M. Glazer, *Acta Crystallogr., B* **1972**, *28*, 3384.
[32] H. Zhang, N. Li, K. Li, D. Xue, *Acta Crystallogr., B* **2007**, *63*, 812.
[33] C. J. Bartel, C. Sutton, B. R. Goldsmith, R. Ouyang, C. B. Musgrave, L. M. Ghiringhelli, M. Scheffler, *Sci. Adv.* **2019**, *5*, eaav0693.
[34] R. D. Shannon, *Acta Crystallogr., A* **1976**, *32*, 751.
[35] M. W. Lufaso, P. M. Woodward, *Acta Crystallogr., B* **2001**, *57*, 725.
[36] R. J. Morelock, Z. J. L. Bare, C. B. Musgrave, unpublished.
[37] I. Yamada, A. Takamatsu, H. Ikeno, *Sci. Technol. Adv. Mater.* **2018**, *19*, 101.
[38] Z. J. L. Bare, R. J. Morelock, C. B. Musgrave, unpublished.
[39] N. Xie, J. Zhang, S. Raza, N. Zhang, X. Chen, D. Wang, *J. Phys. Condens. Matter* **2020**, *32*, 315901.
[40] X. Zhang, C. Pei, X. Chang, S. Chen, R. Liu, Z.-J. Zhao, R. Mu, J. Gong, *J. Am. Chem. Soc.* **2020**, *142*, 11540.
[41] C. J. Bartel, J. M. Clary, C. Sutton, D. Vigil-Fowler, B. R. Goldsmith, A. M. Holder, C. B. Musgrave, *J. Am. Chem. Soc.* **2020**, *142*, 5135.
[42] R. E. Cohen, *Nature* **1992**, *358*, 136.
[43] X.-G. Zhao, G. M. Dalpian, Z. Wang, A. Zunger, *Phys. Rev. B: Condens. Matter* **2020**, *101*, 155137.
[44] F. Eriksson, E. Fransson, P. Erhart, *Adv. Theory Simul.* **2019**, *2*, 1800184.
[45] V. Stevanović, S. Lany, X. Zhang, A. Zunger, *Phys. Rev. B: Condens. Matter* **2012**, *85*, 115104.
[46] G. Hautier, S. P. Ong, A. Jain, C. J. Moore, G. Ceder, *Phys. Rev. B: Condens. Matter* **2012**, *85*, 155208.
[47] O. I. Malyi, A. Zunger, *Appl. Phys. Rev.* **2020**.
[48] A. Steinfeld, *Int. J. Hydrogen Energy* **2002**, *27*, 611.
[49] M. W. Chase, National Institute of Standards and Technology (U.S.), *NIST-JANAF Thermochemical Tables*, American Chemical Society; American Institute of Physics for the National Institute of Standards and Technology, [Washington, DC], Woodbury, NY **1998**.

[50] C. L. Muhich, B. W. Evanko, K. C. Weston, P. Lichty, X. Liang, J. Martinek, C. B. Musgrave, A. W. Weimer, *Science* **2013**, *341*, 540.
[51] C. L. Muhich, S. Blaser, M. C. Hoes, A. Steinfeld, *Int. J. Hydrogen Energy* **2018**, *43*, 18814.
[52] J. E. Park, Z. J. L. Bare, R. J. Morelock, M. A. Rodriguez, A. Ambrosini, C. B. Musgrave, A. H. McDaniel, E. N. Coker, *Front. Energy Res.* **2021**, *9*.
[53] R. J. Morelock, J. Tran, Z. J. L. Bare, A. H. McDaniel, A. W. Weimer, C. B. Musgrave, unpublished.
[54] Z. J. L. Bare, J. T. Tran, R. J. Morelock, A. H. McDaniel, A. W. Weimer, C. B. Musgrave, unpublished.
[55] C. L. Bull, D. Gleeson, K. S. Knight, *J. Phys. Condens. Matter* **2003**, *15*, 4927.
[56] D. V. Karpinsky, I. O. Troyanchuk, K. Bärner, H. Szymczak, M. Tovar, *J. Phys. Condens. Matter* **2005**, *17*, 7219.
[57] X. Qian, J. He, E. Mastronardo, B. Baldassarri, C. Wolverton, S. M. Haile, *Chem. Mater.* **2020**, *32*, 9335.
[58] X. Qian, J. He, E. Mastronardo, B. Baldassarri, W. Yuan, C. Wolverton, S. M. Haile, *Matter* **2021**, *4*, 688.
[59] X. Gao, Z. Jin, R. Hu, J. Hu, Y. Bai, P. Wang, J. Zhang, C. Zhao, *J. Rare Earths* **2021**, *39*, 398.
[60] A. M. Deml, A. M. Holder, R. P. O'Hayre, C. B. Musgrave, V. Stevanović, *J. Phys. Chem. Lett.* **2015**, *6*, 1948.
[61] G. Kresse, J. Hafner, *Phys. Rev. B: Condens. Matter* **1993**, *47*, 558.
[62] G. Kresse, J. Furthmüller, *Comput. Mater. Sci.* **1996**, *6*, 15.
[63] G. Kresse, J. Furthmüller, *Phys. Rev. B: Condens. Matter* **1996**, *54*, 11169.
[64] J. P. Perdew, K. Burke, M. Ernzerhof, *Phys. Rev. Lett.* **1996**, *77*, 3865.
[65] G. Kresse, J. Hafner, *J. Phys. Condens. Matter* **1994**, *6*, 8245.
[66] G. Kresse, D. Joubert, *Phys. Rev. B: Condens. Matter* **1999**, *59*, 1758.
[67] L. Wang, T. Maxisch, G. Ceder, *Phys. Rev. B: Condens. Matter* **2006**, *73*, 195107.